Article

Predicting Phosphorus and Potato Yield Using Active and Passive Sensors

Ahmed Jasim [1,2], Ahmed Zaeen [2], Lakesh K. Sharma [3,*], Sukhwinder K. Bali [4], Chunzeng Wang [5], Aaron Buzza [6] and Andrei Alyokhin [6]

[1] Department of Soil Sciences and Water Resources, Agricultural Engineering College, University of Baghdad, Baghdad 00964, Iraq; ahmed.jasim@maine.edu or ahmedalgburi1981@gmail.com

[2] Department of Ecology and Environmental Sciences, University of Maine, Orono, ME 04469, USA; ahmed.zaeen@maine.edu

[3] Soil and Water Science Department, University of Florida, Gainesville, FL 32611, USA

[4] Department of Agroecology, University of Florida, Gainesville, FL 32611, USA; sukhwinder.bali@ufl.edu

[5] Department of Environmental Science & Sustainability, University of Maine, Orono, ME 04769, USA; chunzeng.wang@maine.edu

[6] School of Biology and Ecology, University of Maine, Orono, ME 04469, USA; aaron.buzza@maine.edu (A.B.); alyokhin@maine.edu (A.A.)

* Correspondence: lakesh.sharma@ufl.edu; Tel.: +1-352-363-7040

check for updates

Abstract: Applications of remote sensing are important in improving potato production through the broader adoption of precision agriculture. This technology could be useful in decreasing the potential contamination of soil and water due to the over-fertilization of agriculture crops. The objective of this study was to assess the utility of active sensors (Crop Circle™, Holland Scientific, Inc., Lincoln, NE, USA and GreenSeeker™, Trimble Navigation Limited, Sunnyvale, CA, USA) and passive sensors (multispectral imaging with Unmanned Arial Vehicles (UAVs)) to predict total potato yield and phosphorus (P) uptake. The experimental design was a randomized complete block with four replications and six P treatments, ranging from 0 to 280 kg P ha^{-1}, as triple superphosphate (46% P_2O_5). Vegetation indices (VIs) and plant pigment levels were calculated at various time points during the potato growth cycle, correlated with total potato yields and P uptake by the stepwise fitting of multiple linear regression models. Data generated by Crop Circle™ and GreenSeeker™ had a low predictive value of potato yields, especially early in the season. Crop Circle™ performed better than GreenSeeker™ in predicting plant P uptake. In contrast, the passive sensor data provided good estimates of total yields early in the season but had a poor correlation with P uptake. The combined use of active and passive sensors presents an opportunity for better P management in potatoes.

Keywords: *Solanum tuberosum* L.; crop circle sensor; GreenSeeker sensor; unmanned aerial vehicle; total potato yield; phosphorus uptake

1. Introduction

Potato (*Solanum tuberosum* L.) is among the most important crops grown in the United States of America (USA) [1]. Maine is ranked ninth among the states in area dedicated to potato production; however, yields are much lower than in Western and Midwestern USA [2]. Phosphorus (P) management is a crucial component of potato production because it impacts early root development and crop yield [3–5]. P plays a vital role in the plant's energy metabolism, such as the synthesis of adenosine triphosphate (ATP) and adenosine diphosphate (ADP) [4,6]. P is also an essential component of phospholipids, phosphoproteins, nucleotides, and coenzymes [7]. It regulates enzymatic metabolism

and activates enzymes such as phosphatase [8]. Under P stress, plants show stunted growth and dark green leaves [9].

The present methods for assessing the amount of P available to growing potato plants are based on soil and plant tissue sampling. Both methods are expensive and labor-intensive. The use of remote sensing techniques to estimate the nutrient status may reduce the labor and lab nutrient analysis cost [10–12]. Remote sensing techniques could provide more intensive data to address the spatial and temporal variations while estimating the crop's nutrient status [13–15].

There are several ways to obtain remotely sensed data, including proximal handheld devices, aircraft-mounted sensors, satellite images, and aerial photography [5,16].

Leaf pigments, including chlorophylls and anthocyanins, absorb and reflect light in specific bands or wavelengths and could easily be estimated with spectral reflectance [14,17]. To date, the remote sensing techniques for the assessment of pigment contents generally involve leaf reflectance (LR) near the visual range (VR) and near-infrared (NIR) absorption maximum of chlorophyll at 675 nm [13,18]. This may be useful for assessing P contents because it plays an essential role in carboxylation, increasing Tchlorophyll levels in plant leaves [19]. The anthocyanin content also provides important information about leaf physiological and structural characteristics [13,20]. It is a water-soluble pigment of higher plants responsible for the red coloration of plant leaves, protecting them from excessive radiation [14]. In leaves, a significant accumulation of anthocyanins is induced due to P stress [21].

Active canopy sensors have adjusted light-emitting diodes that irradiate a plant canopy and estimate the part of the irradiation reflected from the plant canopy that do not depend on the ambient sunlight as utilized in passive sensors [22]. Even though active sensors are working with no solar radiation required, the choice of a light source, the field of view angle, and measuring canopy area could still have a strong effect [23,24]. The sensing area depends on the sensor's structure due to the light signal being typically collimated, sending light from different angles [24]. Therefore, for a particular sensor with a specific viewing angle, the estimating area variation according to the measuring distance is a potentially substantial factor that might influence the rendering of active canopy sensors. However, it is not easy for handheld operating systems to preserve a constant reading distance, even with a fixed sensor position [24].

Active canopy sensors have been utilized on farms by following the sensor companies' guidelines, which may require adjustments for specific crops [23]. The most advantageous wavelengths and vegetation indices vary according to the various crop biophysical parameters and growth stages [25,26]. Several indices, particularly those having red-edge bands, might provide better results than the normalized difference vegetation index (NDVI) for estimating the crop nutrient status [26–28]. The Crop Circle™ ACS-430 (Holland Scientific, Inc., Lincoln, NE, USA) has a red-edge (730 nm) wavelength, which allows this device to calculate various red edge-based vegetation indices [28,29]. Up to now, several studies have compared GreenSeeker™ with Crop Circle™ ACS-210 or ACS-470 [27,30,31]. However, studies with the Crop Circle™ ACS-430 active sensor are limited, especially with phosphorus status. The Crop Circle™ ACS-430 sensor needs more extensive evaluation because it has the unique characteristics of gathering the spectral reflectance measurements recommended by the manufacturer [31,32].

Passive sensors rely on measuring the natural sunlight's reflectance and are often used to scan larger areas than active sensors. They are usually mounted on unmanned aerial vehicles (UAVs), an increasingly widespread tool in production agriculture [33]. Several studies have recently used multispectral and hyperspectral sensors to assess which bands or combinations of bands indicate individual nutrient stress [34,35].

Information obtained using remote sensors could be used to calculate vegetation indices (VIs), which represent normalized differences or ratios of two or more bands; VIs include the normalized difference vegetation index (NDVI), inverse infrared vegetative index (IRVI), normalized difference red-edge (NDRE), leaf area index (LAI), chlorophyll red-edge (CHLRE), blue NDVI (BNDVI), green NDVI (GNDVI), chlorophyll green (CHLGR), and anthocyanin (ANTHO). Of these, the NDVI is

the most widely used vegetation index for determining plant health based on the red wavelength at 660 nm and NIR (700–1200 nm) [36].

Studies on the application of remote sensing techniques to detect P deficiencies are scarce. Leaf reflectance (LR) in the blue band of the visible region (VR) of the electromagnetic spectrum is an excellent measure to estimate the P content in plants [15]. Although P stress had a higher reflectance in the spectrum's yellow and green portions, the red edge did not show a regular shift in chlorophyll absorption at the near-infrared (NIR) region [5,37].

It is crucial to consider the diversity of P spectral signatures of plants to perceive the variability in the signature [38]. The red-edge band (680–760 nm) can be used to predict leaf phosphorus concentration [39] accurately. The NIR region is more sensitive to the plant P status than the visible region [10]. While P stress decreases the LAI, there is no consistent pattern among the different P treatments [40]. The electromagnetic spectrum regions affected by phosphorus were in the range of wavelengths between 400 and 1300 nm [15]. Reflectance at the blue band (445 nm) and NIR (730–900 nm) regions were most suitable to predict P at the early growth stages [11].

The development of new technologies and an improved understanding of the cause-and-effect relationships regarding spatial variability could lead to better management of the applied nutrients, making such measures more economically and environmentally sound [15,35,41]. In this context, the objectives of this study were to compare active and passive sensor performance in detecting P deficiency, total yield, and P uptake in potato throughout the growing season.

2. Materials and Methods

2.1. Site Description

Twelve sites were set up on potato farms in Aroostook County, Maine, USA, in 2018 and 2019 (Tables 1 and 2). The potato cultivars, soil types, and preceding crops are shown in Table 1. The average temperature was between 12 and 20 °C and the precipitation was between 50 and 80 mm. The experimental design at all sites was a randomized complete block with four replications and six P treatments: 0, 56, 112, 168, 224, and 280 kg P ha^{-1} applied as triple superphosphate (46% P_2O_5). In 2018, each experimental unit (plot) was 9.1 m in length and 3.6 m in width, and the rows were spaced at least 0.9 m apart. Nitrogen (N) and potassium (K) were applied equally for all P treatments, with 202 kg N ha^{-1} as urea (46% N) and 224 kg K ha^{-1} as KCl (61% K_2O). In 2019, the same P application rates and resources were applied, and each experimental unit (plot) was 6.1 m in length and 1.8 m in width; the rows were spaced at least 0.9 m apart. Nitrogen was applied equally for all P treatments, with 224 kg N ha^{-1} as ammonium nitrate (34% N), K was applied equally for all P treatments as in 2018. The fertilizers were mixed and applied by the replacement method at planting. Pesticides, such as chlorothalonil, and herbicides, such as Weedar64 (Nufarm) 2,4-D, sourced from Alsip, Illinois, USA, were applied by the farmers as recommended by the University of Maine, Orono, Maine, USA [42].

Table 1. Field experiment information in 2018 and 2019.

Site	Year	Latitude	Longitude	† Soil Type	Planting Date	Harvest Date	Varieties	Previous Crop
Frenchville (FV)	2018	47.2170080	−68.4112920	Coarse-loamy, isotic, frigid Oxyaquic Haplorthods	22 May	12 September	RB	Grain-potato
New Sweden-1 (NS1)	2018	46.9511590	−68.1479550	Fine-loamy, mixed, frigid Typic Haplorthods	29 May	15 October	RB	Clover cover crop
New Sweden-2 (NS2)	2018	46.9529336	−68.1454612	Fine-loamy, mixed, frigid Aquic Haplorthods	30 May	15 October	RB	Clover cover crop
WoodLand (WL)	2018	46.8850498	−68.1256605	Fine-loamy, mixed, frigid Typic Haplorthods	15 May	1 October	RB	Grain-potato
Caribou (CA1)	2018	46.8842966	−68.0292126	Fine-loamy, mixed, frigid Typic Haplorthods	17 May	13 September	RB	Grain-potato
Aroostook Farm-1 (AF1)	2018	46.66601582	−68.0216085	Fine-loamy, mixed, frigid Typic Haplorthods	24 May	14 September	SH	Grasses
Aroostook Farm-2 (AF2)	2018	46.6619155	−68.0209886	Fine-loamy, mixed, frigid Typic Haplorthods	24 May	14 September	RB	Grasses
Aroostook Farm-3 (AF3)	2019	46.66011944	−68.02125	Fine-loamy, mixed, frigid Typic Haplorthods	31 May	20 September	SP	Grasses
Aroostook Farm-4 (AF4)	2019	46.46.6601694	−68.01650278	Fine-loamy, mixed, frigid Typic Haplorthods	31 May	20 September	RB	Grasses
Caribou-1 (CA2)	2019	46.89628611	−68.07754722	Fine-loamy, mixed, frigid Typic Haplorthods	14 May	30 September	RB	Potato, mustard, radish, and potato
Caribou-2 (CA3)	2019	46.89180556	−68.04066667	Fine-loamy, mixed, frigid Typic Haplorthods	28 May	30 September	RB	Potato, white clover, ray, and potato
Limestone (LM)	2019	46.96186944	−67.83323056	Fine-loamy, mixed, frigid Typic Haplorthods	29 May	1 October	RB	Cover crops, clover, oats, and grass

† Information collected from Web Soil Survey (https://websoilsurvey.sc.egov.usda.gov/App/HomePage.htm), 2019. RB: 'Russet Burbank' variety; SH: 'Shepody' variety; SP: 'Superior' variety.

Table 2. Soil chemical properties from the experimental sites in 2018 and 2019.

Site		FV	NS1	NS2	WL	CA1	AF1	AF2	AF3	AF4	CA2	CA3	LM
Growing Years					**2018**						**2019**		
pH		5.9	4.9	5.6	5.8	6.5	6.1	6.4	6.0	6.1	5.4	6.3	5.9
OM [g]	%	4.9	3.1	5.3	4.1	3.7	2.6	4	2.3	3.1	2.6	3.3	1.6
P-MME [a]		19.8	12.2	10.1	16.5	21.2	13.1	21.2	11.4	17.0	17.8	23.8	17.9
P-M3 [b]		379	469	257	356	421	440	421	341	423	586	537	558
$N-NO_3^-$		5	62	2	15	6	4	12	5	6	8	7	3
$N-NH_4^+$	mg nutrient kg soil^{-1}	1	28	25	5	1	15	17	4	6	10	7	19
K-M3 [c]		237	221	151	256	376	300	225	234	160	348	292	230
Fe-MME [d]		10	5.3	9.5	6.8	5.0	2.7	3	4.5	4.8	8.2	4.1	4.7
Fe-M3 [e]		309	438	390	317	343	388	375	334	368	483	394	396
Al-M3 [f]		1735	1595	1395	1547	1595	1590	1444	1600	1594	1789	1796	1822
CEC − MME [h]	meq 100 g^{-1}	7.3	8.1	8.8	7.3	7.9	5.9	7.9	5.4	6.3	7.2	7.0	4.6

Modified Morgan Extraction (MME); [a] P extracted by MME (P-MME); [b] Mehlich 3 (M3); Mehlich 3 soil test P (P-M3); [c] K extracted by M3 (K-M3); [d] Iron extracted by MME (Fe-MME); [e] Iron extracted by M3 (Fe-M3); [f] Aluminum extracted by M3 (Al-M3); [g] Organic Matter (OM); [h] Cation exchangeable capacity extracted by MME (CEC − MME).

2.2. Soil Sampling and Analysis

Before planting, soil samples were collected from the twelve sites (Table 1) using a 2-cm diameter stainless probe. There were five subsamples collected at a depth of 0 to 25 cm for pH, organic matter, P, $N-NO_3^-$, $N-NH_4^+$, and K analysis (Table 2). The soil samples were air-dried and ground to pass through 2-mm sieves. Soil pH was estimated using a 1:1 soil: deionized water solution and a pH meter (pH robot is a labfit AS3000; company HQ located in Perth, Australia), with an appropriate electrode (s) [43]; the organic matter was determined using loss of weight on ignition [44]. The phosphorus (P) was analyzed by Mehlich 3 extraction, followed by analyzing the filtrate via the Inductively Coupled Plasma (ICP) (Spectro Genesis, Kleve, Germany) method [45]. The P and K levels were determined by Modified Morgan Extraction (MME) and estimated within the linear range on the ICP. The $N-NO_3^-$ was measured by using an automated ion analyzer and the recommended ratio of 1:10 (5 g soil; 50 mL extractant (0.01 M CaSO4, 2 M KCl)) [46]. The $N-NH_4^+$ was measured via KCl extraction [47]. The University of Maine Soil Laboratory, Orono, Maine, USA, analyzed the soil samples.

2.3. Plant Sampling and Analysis

One petiole and leaflet (whole leaves) was collected, at the tuber initiation stage (60 days after the planting date), from each potato plant, thus, four plants were collected from each sub-plot for the phosphorus analysis. The petioles and leaflets were taken from the fourth and fifth fully expanded leaves from the plant top [48], dried in an oven with air circulation at 65 °C for 96 h, and ground. Subsequently, the samples were turned into ash at 550 °C for 5 h in a muffle furnace. The obtained ash was dissolved in 50% HCl on a hot plate and analyzed using ICP [49]. The University of Maine Soil Laboratory analyzed the plant samples. Phosphorus uptake (kg ha^{-1}) was calculated by multiplying the dry matter of the petioles and leaflets by the percentage of phosphorus content (%) as follows:

$$\text{Phosphorus uptake (kg ha}^{-1}) = \frac{\text{Dry matter of petioles and leaflets (kg ha}^{-1}) \times \text{Phosphorus content (\%)}}{100} \tag{1}$$

2.4. Potato Harvest

At the harvest time (after 130 to 140 days from planting; Table 1), the tubers were dug using a two-row digger and then handpicked manually from a 5.5 m^2 area within the central rows of each

plot. Individual plots were harvested separately to remove possible border effects. Fresh tubers were graded and weighed to determine the total potato tuber yield (Mg ha^{-1}).

2.5. Sensor Description and Sensing Procedure

2.5.1. Active Sensors

We used the sensors GreenSeeker™ (GS; Trimble Navigation Limited, Sunnyvale, CA, USA) and Holland Scientific Crop Circle™ ACS 430 (CC; Holland Scientific, Inc., Lincoln, NE, USA). The GS sensor was used to measure incident light and reflected light from plants at 660 ± 15 nm (red) and 770 ± 15 nm (NIR) to obtain the NDVI and IRVI [50]. Sensor readings were downloaded by connecting the sensor to a laptop computer. The GreenSeeker™ (GS) emits two wavelengths of reflectance light: 660 ± 15 nm (red band) and 770 ± 15 nm (NIR band). The GS active sensor light would be emitted from diodes in alternate bursts, thus, the red and NIR bands pulse for 1 ms (1 millisecond) at 40,000 Hz. Each burst from the diodes would obtain up to 40 pulses before pausing for the other diode to emit its radiation (plus 40 pulses). The lighted area is 60 cm wide by 1 cm long, with the extending dimension basically positioned vertically to the direction of the GS sensor in the field movement.

The CC sensor was simultaneously used to measure the crop/soil reflectance at 670 nm, 730 nm, and 780 nm. The data were collected using a Holland Scientific GeoSCOUT GLS-400 (Holland Scientific, Inc., Lincoln, NE, USA) datalogger and downloaded to a laptop computer. The CC yielded several vegetation indices, such as NDRE (normalize differences red-edge), NDVI, and the leaf area index (LAI), obtaining as the sensor output chlorophyll red edge (CHLRE) (Table 3). The CC-430 active sensor incorporates three fixed wavebands. The field of view (FOV) was an oval of ~30° by ~14° range. The readings would be collected at one measurement height (60 cm) above the potato canopy at 10 Hz (10 readings/s) when moving at a constant speed in each experimental unit. The sensor path was parallel to the potato rows with the beam of reflected light positioned vertically to the potato rows.

Each sensor recorded about 45–60 readings during one passing through the plot and collected readings from the two middle rows. The reading values were averaged and organized using the in-house Excel macro option for Visual Basic (Microsoft Excel 2020, Version 16.43, NC, USA). For June to August, thirteen active sensing dates took place in each of the twelve experimental sites: 25 June, 1 July, 9 July, 12 July, 18 July, 22 July, 25 July, 1 August, 5 August, 13 August, 16 August, 20 August, and 23 August. The sensing dates were excluded from the results when there was no significant model fit to the data.

2.5.2. Passive Sensors

Unmanned Aerial Vehicle Image Acquisition and Processing

In 2018, two DJI Phantom 4 UAVs (Shenzhen, Guangdong, China) (Figure 1a) were used for image acquisition. One had a NIR camera/sensor and was used to obtain the NIR images (Figure 1b). The other had a regular camera/sensor used to collect the visible-color images of the red, green, and blue bands (Figure 1c). The gimbal controlled the UAV movement (pitch and roll) throughout the flight [51]. In 2019, A DJI Inspire 2 UAV (Shenzhen, Guangdong, China) with a portable Altum multispectral sensor (MicaSense, Seattle, WA, USA) was used to collect the multispectral data (Figure 1d). Figure 1e shows how the Altum sensor integrates a radiometric thermal camera with five high-resolution narrow bands and produces advanced thermal multispectral and high-resolution imagery in one flight for the advanced analytic spectral bands: blue (475 nm center, 20 nm bandwidth), green (560 nm center, 20 nm bandwidth), red (668 nm center, 10 nm bandwidth), red-edge (717 nm center, 10 nm bandwidth), NIR (840 nm center, 40 nm bandwidth), and thermal (LWIR thermal infrared 8000 to 14,000 nm, radiometrically calibrated). The altitude for the UAV was 75–80 m; the flight duration was based on the field size, which was between 8 and 12 min; the resolution was 3.2 cm pixels^{-1}; the overlap was 90/90;

the image count was 86 to 112 images, depending on the distance of the field; and maximum speed was 2.7 m/s. The flight was performed between 10:00 a.m. and 2:30 p.m. local time in the study area.
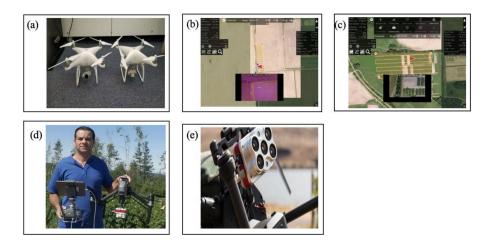

Figure 1. (**a**) The two DJI Phantom 4 UAVs used in 2018. (**b**) Drone flight with a NIR camera. (**c**) Drone flight with an RGB camera. (**d**) DJI Inspire 2 drone and the Altum sensor. (**e**) The Altum sensor.

A certification of authorization was obtained from the United States Federal Aviation Administration (US-FAA) in Lincoln, Nebraska, USA, for the DJI Phantom 4 and DJI Inspire 2 flights. In 2018, images were taken by a Sony 4K camera (Shenzhen, Guangdong, China) with a 12 megapixel 1/2.3″ complementary metal-oxide-semiconductor (CMOS) sensor (4000 × 3000 pixels). Both camera settings were maximum wide-angle identical to a 28 focal length (35 mm format equivalent), with auto exposure bracketing, auto speed, autofocus, auto white balance, f/2.8 aperture, and focus at infinity ∞.

In 2019, the Inspire 2 was equipped with an Altum sensor with a spatial resolution of 5.2 cm per pixel (per earth observing (EO) band) at 120 m (400 ft) AGL (above ground level), 81 cm per pixel (thermal) at 120 m, 1 capture per second (all bands), 12-bit RAW, and FOV (field of view) of 48° × 37° (multispectral) and 57° × 44° (thermal): FL (focal length) 8 mm (multispectral) and 1.77 mm (thermal).

Acquisition points were generated in the field and used as a waypoint for the flight path. In each flight operation, a steady ambient lighting condition was attempted (sunny days). In all flight campaigns, Map Pilot for DJI (Man Made Easy, Shenzhen, Guangdong, China) was used. Maps and waypoints were generated and saved for the next flights. For the Altum sensor, a calibrated reflectance panel was used to calibrate images.

Image calibration was implemented before each flight using an automatic panel detection mode that automatically recognizes and obtains the calibration panel image. The live view tab of the passive sensor configuration page displays a live image and detects the reflectance panel and quick response (QR) mode after selecting the QR button using the sensor camera. The drone-sensor was held at least 1 m above the calibrated reflectance panel to obtain the image from centering the panel and QR code in the field of view. Once the sensor detected the panel, it sent a unique sound and flashed the blue LED light, indicating that the image was captured. To ensure that the calibrated image was taken, the calibrated panel should be placed flat on the ground and far from any objects that could impact the light and illuminate the captured image. The operator (drone pilot) stands in front of the calibrated panel, and the sunshade is directed at the operator's back. Shadows should be eliminated when the panel is on the ground to prevent invalidated reflectance compensation readings.

The experiment's images were uploaded via Agisoft Metashape software (Agisoft LLC, St. Petersburg, Russia) once for all bands. Photos were uploaded, including the reflectance calibration images. The calibrated images were selected and prompted to upload the calibration from the comma separated values (CSV) file provided by MicaSense (MicaSense, Seattle, WA, USA); this CSV file has all the calibration values corresponding to the MicaSence radiometric panel, obtained from the MicaSense website on https://micasense.com/prv/. Therefore, in the Agisoft Metashape processing software,

the reflectance option and the sun sensor in the calibrated reflectance dialog were selected to perform the calibration based on panel data and image meta information.

Drones had the Downwelling Light Sensor (DLS), which provides reliable and accurate radiometric data. In this study, the drones' DLS provided a sun sensor that measures the solar irradiance at the drone's top. It is an important element to minimize the change in the environmental light conditions. The DLS normalized the data to the standard conditions.

An orthomosaic was created from images in 2018 using the Pix4DMapper software (Pix4D mapper, Lausanne, Switzerland) [52]. The Agisoft Metashape professional software 1.6.3 [53] was used to process the images from 2019. Rectifications to the camera's view distortions were performed, and the images were stitched together to create a geo-referenced orthomosaic (GeoTIFF). The GeoTIFF image for each flight was uploaded in ArcGIS (Version 10.3; Esri Headquarters, Redlands, CA, USA) [54]. In ArcGIS, polygons were generated to represent each experimental plot (Figure 2). All processing was performed with an HP laptop (Spring, TX, USA), with a 4-core Intel 10TH Gen i7-1065G7 CPU @ 1.30 GHz (max 1.5 GHz), 16 GB memory, 1TB SSD + 32GB Optane, and NVIDIA GeForce RTX 2070 GPU(Palo Alto, CA, USA).
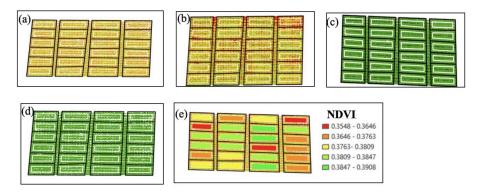

Figure 2. The experimental field at the early leaf stage: (**a**) black boxes indicate experimental plots, and white boxes within the black boxes indicate the buffer area for each plot and for two middle rows, manually; (**b**) boxes indicate NDVI for all pixels and plots; (**c**) manually, non-plant pixels were removed from the image using reclassification; (**d**) non-plant pixels were excluded by multiplying (**c**) by (**b**) to obtain the NDVI image just for plant pixels; (**e**) NDVI values for each plot (average of two middle rows) in the field, in this photo, zonal statistics (spatial analyst) in Arc GIS is shown in this photo to differentiate the experiment plots, automatically. In our study, we used zonal statistics as a table to obtain the means values. The same procedure was done for all passive vegetation indices and plant pigments.

For June to August, eight passive sensing dates took place in each of the twelve experimental sites: 25 June, 1 July, 9 July, 16 July, 22 July, 29 July, 14 August, and 23 August. Some flight operation dates were excluded from the results when no model provided a significant fit to the data.

Visible Bands and NIR Vegetation Indices

The digital numbers (DN) converted reflectance was calculated by converting the *.TIF files to float files (*.FLT) (Figure 3). The VI equations in Table 3 were used as input to the raster calculator to calculate the VIs. To acquire the average for each plot (two middle rows), we used the command "Zonal statistics as a table". These processes were repeated for all the VIs and each orthomosaic photo (GeoTIFF) by employing an iterator.
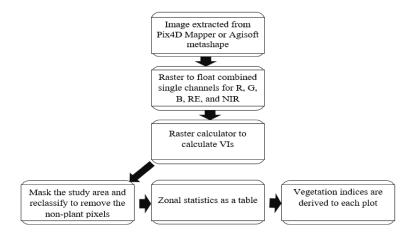
Figure 3 flowchart:

Image extracted from Pix4D Mapper or Agisoft metashape

↓

Raster to float combined single channels for R, G, B, RE, and NIR

↓

Raster calculator to calculate VIs

↓

Mask the study area and reclassify to remove the non-plant pixels → Zonal statistics as a table → Vegetation indices are derived to each plot

Figure 3. Data processing workflow for GeoTIFF from the RGB, NIR, and thermal Altum sensor images captured by the Phantom DJI and Inspire 2.

Table 3. Summary of the spectral reflectance data used in this study.

Vegetation Indices	Formula	Vegetation Index Resource	Citations
NDVI [a]	(NIR − R)/(NIR + R)	CC, GS, and UAVs	[36]
NDRE [b]	(NIR − Red edge)/(NIR + Red edge)	CC	[55]
CHLGR [c]	(NIR/G) − 1	UAVs	[14]
CHLRE [d]	(NIR/Red edge) − 1	CC	[14]
BNDVI [e]	(NIR − B)/(NIR + B)	UAVs	[56]
GNDVI [f]	(NIR − G)/(NIR + G)	UAVs	[56]
ANTHO [g]	R/G	UAVs	[13]
IRVI [h]	R/NIR	GS	[50,57]

[a] NDVI: Normalized difference vegetation index; [b] NDRE: Normalized difference red-edge; [c] CHLGR: Chlorophyll green; [d] CHLRE: Chlorophyll red-edge; [e] BNDVI: Blue normalized difference vegetation index; [f] GNDVI: Green normalized difference vegetation index; [g] ANTHO: Anthocyanin; R: red band; G: green band; B: blue band; NIR: near-infrared; CC: Crop Circle™ sensor; GS: GreenSeeker™; [h] IRVI: Inverse infrared vegetative index; UAVs: Unmanned aerial vehicles.

2.6. Statistical Analysis

Because the sensing dates were the same for both years, the data were pooled for each date. As interpreted from the handheld sensors and the drones, both the active and passive sensors showed some skewing degree, indicating the potential benefits of data diagnostics and transformation, such as a log transformation. These analyses were performed on both transformed and untransformed data. All the data were analyzed using RStudio software (Version 1.3.1073; Boston, MA, USA).

2.7. Multiple Linear Regression Model Diagnostics

2.7.1. Criteria for Evaluation of a Subset of Predictor Variables

Both untransformed and transformed models were evaluated by adjusted R^2 (R^2_{adj}), Akaike's Information Criterion (AIC), Corrected Akaike's Information Criterion (AICc), Bayesian Information Criterion (BIC), and Prediction Sum of Squares (PRESS), as follows:

Adjusted $R^2 = R^2_{adj}$

$$R^2_{adj} = 1 - \frac{\frac{SSE}{(n - p - 1)}}{\frac{SST}{(n - 1)}} \tag{2}$$

$$SSE = \sum_{i=1}^{n} (yi - y)^2 \tag{3}$$

$$SST = \sum_{i=1}^{n} (yi - y)^2 \tag{4}$$

where R^2_{adj} represents the adjusted R^2; SSE is the error sum of squares; y_i is the ith observation; n is the number of observations; y is the mean of the n observations; SST the total sum of squares; y is the predicted value of y; and p is the number of predictors. R^2_{adj} was implemented in R using the $R_{sq.adj}$ package.

Akaike's Information Criterion AIC

$$AIC = (n \log (SSE/n) + 2p + other\ terms \tag{5}$$

where n is the number of observations; SSE is the error sum of squares; and p is the number of predictors. Other terms are independent of the error sum of squares and p. The smaller AIC values indicate the better model fit.

The AIC package was implemented in R software as AIC < - sapply (1:m, function (x) round (extractAIC (om [[x]], k = 2) [2], 2)). The other terms were independent of SEE and P and the same for every model.

Corrected Akaike's Information Criterion AICc

AICc is developed to overcome the model complexity when the AIC is not strong enough. In the multiple linear regression model, AICc is obtained as shown in Equation (6):

$$AICc = AIC + \frac{2\,(p+2)(p+3)}{n-p-1} \tag{6}$$

where n is the number of observations and p is the number of predictors. The R package sapply (1:m, function (x) round (extractAIC (om [[x]], k = 2) [2] + 2 *npar[x] *(npar [x] + 1)/(n-npar [x] + 1), 2)) was used for the analysis.

Bayesian Information Criterion BIC

The BIC is often used to select variables in multiple regression problems. In this study, BIC was used to determine the best model (where regression models were a variable subset). The following equation can obtain the BIC:

$$BIC = -2 \log L\,(\beta_0, \dots, \beta_p, \acute{o}^2_{MLE}|Y) + K \log n \tag{7}$$

where K = p + 2, the number of parameters estimated in the regression model; and MLE is the maximum likelihood estimation used to estimate the probability distribution parameters by maximizing a likelihood function.

Prediction Sum of Squares (PRESS)

The PRESS summarizes the multiple linear regression model's fit to a sample of observations using the fitted regression function to obtain the predicted value. PRESS is shown in Equation (8):

$$PRESS = \sum_{i=1}^{n} (yi - yi(i))^2 \tag{8}$$

where y_i is the predicted value for the ith subject; and $y_i - y_i$ is the prediction error for the ith subject.

2.7.2. Generalized Linear Model (GLM)

For the GLM, we first tested the overall correlation between the total potato yield and the vegetation indices for active and passive sensors. In the untransformed model, we selected the best predictors ($p < 0.05$) and excluded the non-significant predictors to increase the adjusted R^2 and minimize the subsection variables; the multiple linear regression approach was used with the transformed model.

Backward and forward stepwise regression was used with all vegetation indices for the active and passive sensors to guide which model might have the minimum AIC and BIC in predicting total potato yield and phosphorus uptake. Finally, models were established based on the maximized adjusted R^2 to minimize all possible selections. These vegetation indices were used to predict the total potato yield and phosphorus uptake based on the GLM, as shown in Equation (9):

$$Y_i = \beta_0 + \beta_1 X_{i1} + \ldots \ldots \ldots + \beta_n X_{in} + \varepsilon_i \tag{9}$$

where Y_i indicates the response variable; X_{in} represents the predictor variables; β_0, β_1, and β_n are the parameters of the model; and ε_i is the error term.

Active Sensor Transformation Models Based on the Generalized Linear Model (GLM)

The active sensors' vegetation indices were correlated linearly amongst the predictors and the dependent variables, as shown in Equations (10) and (11) for the Crop Circle™ sensor outputs:

$$\text{Total potato yield} = \beta_0 + \beta_1 \, NDRE + \beta_2 \, NDVI + \beta_3 \, CHLRE + \beta_4 \, LAI + \varepsilon_i \tag{10}$$

$$\text{Phosphorus uptake} = \beta_0 + \beta_1 \, NDRE + \beta_2 \, NDVI + \beta_3 \, CHLRE + \beta_4 \, LAI + \varepsilon_i \tag{11}$$

Calculations for the GreenSeeker™ active sensor are shown in Equations (12) and (13):

$$\text{Total potato yield} = \beta_0 + \beta_1 \, NDVI + \beta_2 \, IRVI + \varepsilon_i \tag{12}$$

$$\text{Phosphorus uptake} = \beta_0 + \beta_1 \, NDVI + \beta_2 \, IRVI + \varepsilon_i \tag{13}$$

The transformation model was used based on the Box-Cox transformation approach 1 for the Crop Circle™ active sensor; we applied the response and explanatory log-transformed models in Equations (14) and (15):

$$\text{Log Total potato yield} = \beta_0 + \beta_1 \, log \, NDRE + \beta_2 \, log \, NDVI + \beta_3 \, log \, CHLRE + \beta_4 \, log \, LAI + \varepsilon_i \tag{14}$$

$$\text{Log Phosphorus uptake} = \beta_0 + \beta_1 \, log \, NDRE + \beta_2 \, log \, NDVI + \beta_3 \, log \, CHLRE + \beta_4 \, log \, LAI + \varepsilon_i \tag{15}$$

For the GreenSeeker™ active sensor, the same approach was used, as shown in Equations (16) and (17):

$$\text{Log Total potato yield} = \beta_0 + \beta_1 \, log \, NDVI + \beta_2 \, log \, IRVI + \varepsilon_i \tag{16}$$

$$\text{Log Phosphorus uptake} = \beta_0 + \beta_1 \, log \, NDVI + \beta_2 \, log \, IRVI + \varepsilon_i \tag{17}$$

Passive Sensor Transformation Models Based on the Generalized Linear Model (GLM)

For the passive sensor vegetation indices, a multiple linear regression was generated, as shown in Equations (18) and (19):

$$\text{Total potato yield} = \beta_0 + \beta_1 \, NDVI + \beta_2 \, GNDVI + \beta_3 \, BNDVI + \beta_4 \, CHLGR + \beta_5 \, LAI + \varepsilon_i \tag{18}$$

$$\text{Phosphorus uptake} = \beta_0 + \beta_1 \, NDVI + \beta_2 \, GNDVI + \beta_3 \, BNDVI + \beta_4 \, CHLGR + \beta_5 \, LAI + \varepsilon_i \tag{19}$$

Due to the low vegetation indices values for the passive sensors compared to the active sensors, we used only the response log, as shown in Equations (20) and (21):

$$\text{Log Total potato yield} = \beta_0 + \beta_1 \, NDVI + \beta_2 \, GNDVI + \beta_3 \, BNDVI + \beta_4 \, CHLGR + \beta_5 \, LAI + \varepsilon_i \tag{20}$$

$$\text{Log Phosphorus uptake} = \beta_0 + \beta_1\,NDVI + \beta_2\,GNDVI + \beta_3\,BNDVI + \beta_4 \\ CHLGR + \beta_5\,LAI + \varepsilon_i \tag{21}$$

3. Results

3.1. Active Sensors

3.1.1. Crop Circle™

Total Potato Yield and Phosphorus Uptake Models

Based on the adjusted R^2, p value, AIC, AICc, BIC, and PRESS values (Table 4), the most affected total potato yield variables were NDRE, NDVI, and CHLRE.

The models for the first sensing date, 25 June, and the last significant sensing date, 1 August, showed the highest adjusted R^2 values (0.36 and 0.31), respectively. The last sensing date (1 August) model was improved after transforming (R^2_{adj} = 0.32). The lowest R^2_{adj} values (0.10) were obtained for the fourth, sixth, and seventh sensing dates, 12 July, 22 July, and 25 July, respectively. At the first sensing date (25 June), the multiple regression model applied to the test data set had the best R^2_{adj} (0.36) with the smallest AICc and BIC values. Several models were improved following the transformation. All the final regression models were statistically significant (all p values < 0.0001), except for 22 July's untransformed model (Table 4).

The P uptake models had the best fit on the third sensing date, based on the highest R^2_{adj} value (0.60) and the lowest validation criteria (Table 5). The fourth and fifth sensing dates showed a weak correlation between the response variable (P uptake) and predictors (NDVI, NDRE, LAI, and CHLRE). The NDVI was the only vegetation index that impacted P uptake on the fourth sensing date (12 July), with an R^2_{adj} of 0.32. There were no significant responses for the last six sensing dates; therefore, the equations were excluded from Table 5.

Relationships between the Actual and Predicted Variables

The strongest relationship between the actual and predicted total potato yields was observed for both the transformed and untransformed models on 25 June (Figure 4a,b) and on 1 August (Figure 4e,f). In contrast, the weakest relationship was found for the untransformed model on July 22 (Figure 4c). However, transforming the data increased the variation explained by the model (Figure 4d).

The strongest relationship between the actual and the predicted P uptake was detected on 9 July for both the transformed and untransformed data (Figure 5a,b). In contrast, the weakest relationship was foreseen on 25 July (Figure 5d). The transformation had little effect on the model fit on any of the sensing dates (Figure 5).

3.1.2. GreenSeeker™

Total Potato Yield and Phosphorus Uptake Models

There was little correlation between the observed and predicted values until August 5 (Table 6). The transformations increased the coefficients of determination values on 5 August, 16 August, and 20 August (Table 6).

On the contrary, the models best predicted phosphorous uptake early in the season (Table 7).

Table 4. Total potato yield models with the adjusted coefficient of determination (R^2_{adj}), *p* Value, AIC, AICc, BIC, and PRESS for Crop Circle™.

Active Sensing	Model Transformation	Model	R^2_{adj}	*p* Value	AIC	AICc	BIC	PRESS
25 June	Untransformed Model	Yield = 43.47 − 13018.16 NDRE + 184.89 NDVI + 6254.57 LAI − 2353 CHLRE	0.36	<0.0001	462.60	463.14	476.34	5810.70
	Transformed Model	log Yield = 0.8171 − 2.2036 log (NDRE) + 0.0546 log (NDVI) + 1.3229 log (CHLRE)	0.29	<0.0001	−321.24	−320.51	−307.30	8.24
12 July	Untransformed Model	Yield = 35.18 + 235.42 NDRE − 75.41 NDVI − 85.59 LAI + 69.72 CHLRE	0.10	<0.0001	1206.65	1206.95	1224.97	18,935.50
	Transformed Model	log Yield = 1.4055 − 1.0264 log (NDRE) − 1.1538 log (NDVI) + 1.2319 log (CHLRE)	0.15	<0.0001	−751.81	−751.51	−733.49	21.18
18 July	Untransformed Model	Yield = 73.62 + 308.90NDRE − 49.16NDVI − 390.37LAI + 282.02 CHLRE	0.05	0.001	613.81	614.10	632.12	10,212.22
	Transformed Model	log Yield = 2.9995 − 6.0205 log (LAI) + 5.0766 log (CHLRE)	0.10	<0.0001	−732.97	−732.76	721.98	22.46
22 July	Untransformed Model	Yield = 30.785 + 22.326 NDRE − 85.739 NDVI	0.10	0.0040	8.16	848.45	856.61	3205.26
	Transformed Model	log Yield = −3.442 − 5.034 log (NDRE) − 4.416 log (LAI) + 8.481 log (CHLRE)	0.23	<0.0001	−313.20	−312.47	−301.33	8.88
25 July	Untransformed Model	Yield = 15.363 + 118.08 NDRE − 24.02 NDVI	0.10	<0.0001	1205.52	1205.66	1216.51	18,852.67
	Transformed Model	log Yield = 3.8273 + 0.6015 log (NDRE) − 0.8466 log (NDVI) + 0.3850 log (LAI)	0.11	<0.0001	−739.30	−739.09	−724.65	22.01
1 August	Untransformed Model	Yield = 50.38 − 449.03 NDRE + 41.97 NDVI + 53.31 CHLRE	0.31	<0.0001	1132.39	1132.60	1147.04	14,534.85
	Transformed Model	log Yield = −5.1378 − 6.4729 log (NDRE) + 1.7950 log (NDVI) + 3.7054 log (LAI)	0.32	<0.0001	−818.74	−818.52	−804.08	16.74

NDVI: Normalized difference vegetation index; NDRE: Normalized difference red-edge; LAI: Leaf area index; CHLRE: Chlorophyll red-edge; Akaike's Information Criterion (AIC); Akaike's Information Corrected Criterion (AICc); Bayesian Information Criterion (BIC). PRESS: Prediction sum of squares. Significantly different at *p* < 0.05.

Table 5. Phosphorus uptake (kg ha $^{-1}$) models with adjusted coefficients of determination (R^2_{adj}), *p* Value, AIC, AICc, BIC, and PRESS for Crop Circle™.

Active Sensing	Model Transformation	Model	R^2_{adj}	*p* Value	AIC	AICc	BIC	PRESS
9 July	Untransformed Model	PU = 2.36 − 283.44 NDRE + 38.84 NDVI + 122.80 LAI − 74.58 CHLRE	0.60	<0.0001	78.36	78.66	96.68	378.00
	Transformed Model	log PU = 4.8175 + 2.4835 log (NDRE) + 2.3266 log (NDVI) − 4.1608 log (LAI)	0.62	<0.0001	−428.96	−428.75	−414.31	66.01
12 July	Untransformed Model	PU = 5.7030 +19.8137 NDRE − 13.6055 NDVI	0.32	<0.0001	232.61	232.75	243.60	643.97
	Transformed Model	log PU = −0.1454 − 1.1422 log (NDVI)	0.28	<0.0001	−245.71	245.62	238.38	122.32
18 July	Untransformed Model	PU = 4.915 − 118.070 NDRE + 73.902 LAI − 43.421 CHLRE	0.26	<0.0001	264.89	265.10	279.54	702.90
	Transformed Model	log PU = −19.180 − 14.841 log (NDRE) − 10.736 log (CHLRE) + 22.227 log (LAI)	0.23	<0.0001	−224.50	−224.28	−209.84	131.69
25 July	Untransformed Model	PU = 10.59 − 37.47 NDRE − 3.98 NDVI + 4.49 LAI	0.10	<0.0001	315.79	316.00	330.44	858.10
	Transformed Model	log PU = −1. 2754 − 1.6569 log (NDRE) + 0.5670 log (NDVI)	0.07	<0.0001	−161.71	−161.57	150.72	157.06

PU: Phosphorus uptake; NDVI: Normalized difference vegetation index; NDRE: Normalized difference red-edge; LAI: Leaf area index; CHLRE: Chlorophyll red-edge; Akaike's Information Criterion (AIC); Akaike's Information Corrected Criterion (AICc); Bayesian Information Criterion (BIC). Significantly different at *p* < 0.05. PRESS: Prediction sum of squares.
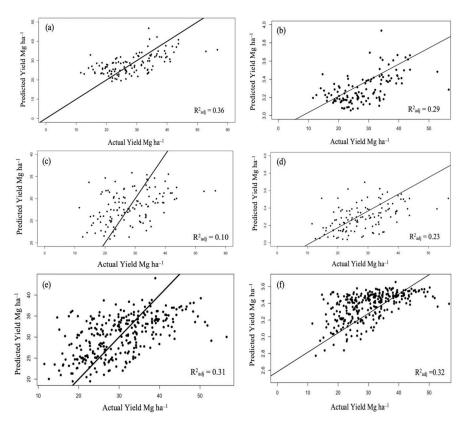
Figure 4. Relationship between the actual and predicted total potato yield for the sensing dates of (**a**) 25 June, the untransformed model; (**b**) 25 June, the transformed model; (**c**) 22 July, the untransformed model; (**d**) 22 July, the transformed model; (**e**) 1 August, the untransformed model; (**f**) 1 August, the transformed model.
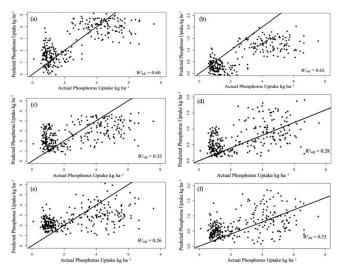

Figure 5. Relationship between actual and predicted phosphorus for (**a**) 9 July, the untransformed model; (**b**) 9 July, the transformed model; (**c**) 12 July, the untransformed model; (**d**) 12 July, the transformed model; (**e**) 18 July, the untransformed model; (**f**) 18 July, the transformed model.

Relationships between the Actual and Predicted Variables

The most robust relationship between the actual and predicted total potato yield was obtained by the model using the transformed data on August 5 (Figure 6b). The weakest relationship with total potato yield was found for an untransformed model on 16 August (Figure 6c).
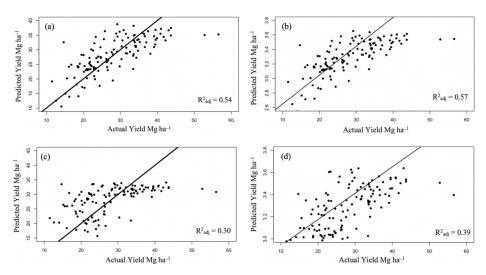
Figure 6. Relationship between the actual and predicted total potato yield for both sensing dates in 2018 and 2019: (**a**) 5 August, the untransformed model; (**b**) 5 August, the transformed model; (**c**) 16 August, the untransformed model; (**d**) 16 August, the transformed model.

For the P uptake, the coefficient of determination was comparable to those obtained for potato yields. The most robust relationship was obtained for the untransformed model on 1 July (Figure 7a). Transformations did not have a major input on model performance.
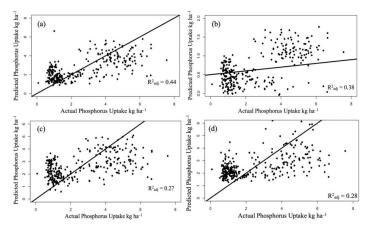

Figure 7. Relationship between the actual and predicted phosphorus uptake for (**a**) 1 July, the untransformed model; (**b**) 1 July, the transformed model; (**c**) 12 July, the untransformed model; (**d**) 1 August, the untransformed model.

3.2. Passive Sensors

3.2.1. Total Potato Yield and Phosphorus Uptake Models

Models constructed using the data from the passive sensors provided a relatively good prediction of the total potato yield throughout the growing season, starting on the earliest sensing date of 25 June, with coefficients of determination fluctuating around 0.50 (Table 8). The vegetation indices that most frequently predicted total potato yield were NDVI, CHLGR, and ANTHO. Transforming the data did not result in better-fitted models (Table 8). Total potato yield was negatively correlated with ANTHO on the first drone flight date (June 25).

P uptake models explained very little variation observed in our experiments (Table 9). Once again, transforming the data did not produce models with meaningfully higher coefficients of determination. The outcomes were consistent across all sensing dates (Table 9).

Table 6. Total potato yield models with an adjusted coefficient of determination (R^2_{adj}), *p* Value, AIC, AICc, BIC, and PRESS for GreenSeeker™.

Active Sensing	Model Transformation	Model	R^2_{adj}	*p* Value	AIC	AICc	BIC	PRESS
9 July	Untransformed Model	Yield = −110.84 + 164.58 NDVI + 158.86 IRVI	0.09	<0.0001	1218.50	1218.64	1225.82	19,116.69
	Transformed Model	log Yield = 3.5376 + 0.2236 log (NDVI)	0.06	<0.0001	−726.95	−726.86	−719.62	23.04
12 July	Untransformed Model	Yield = −23.14 IRVI + 42.91	0.04	0.0006	1223.27	1223.36	1230.60	20,105.90
	Transformed Model	log yield = 3.1826 − 0.1505 log (IRVI)	0.04	0.00025	−721.64	721.56	−714.32	23.48
18 July	Untransformed Model	Yield = 232.43 NDVI + 262.87IRVI − 185.52	0.09	<0.0001	8.11	2028.17	2042.68	19,132.28
	Transformed Model	log Yield = 4.7863 + 1.9445 log (NDVI) + 0.4395 log (IRVI)	0.05	0.009	−724.90	−724.67	−713.28	23.32
25 July	Untransformed Model	Yield = 144.31 NDVI+ 164.67 IRVI − 104.97	0.04	0.0018	8.34	2044.58	2059.09	20,203.57
	Transformed Model	log Yield = 3.717 + 0.7188 log (NDVI) + 0.0801 log (IRVI)	0.02	0.016	−714.36	−714.22	−703.38	24.04
5 August	Untransformed Model	Yield = −27.274 + 75.170 NDVI	0.54	<0.0001	421.08	421.28	426.66	4010.02
	Transformed Model	log Yield = 3.9112 + 1.9875 log (NDVI)	0.57	<0.0001	−384.15	−383.94	−378.57	4.88
16 August	Untransformed Model	Yield = −4.849 + 43.499 NDVI	0.30	<0.0001	470.08	470.28	475.65	6028.96
	Transformed Model	log Yield = 1.4134 − 1.1571 log (NDVI) − 0.7660 log (IRVI)	0.39	<0.0001	−340.05	−339.71	−331.69	7.03
20 August	Untransformed Model	Yield = −183.88 + 229.21NDVI + 250.35 IRVI	0.32	<0.0001	468.49	476.51	476.51	5884.35
	Transformed Model	log Yield = 1.2353 − 1.2632 log (NDVI) − 0.8222 log (IRVI)	0.44	<0.0001	−351.34	−351.00	−342.97	6.43

NDVI: Normalized difference vegetation index; IRVI: Inverse infrared vegetative index; Akaike's Information Criterion (AIC); AICc: Akaike's Information Corrected Criterion; BIC: Bayesian Information Criterion. Significantly different at *p* < 0.05. PRESS: Prediction sum of squares. Significantly different at *p* < 0.05.

Table 7. Phosphorus uptake (kg ha^{-1}) models with adjusted coefficients of determination (R^2_{adj}), *p* Value, AICc, BIC, and PRESS for GreenSeeker™.

Active Sensing	Model Transformation	Model	R^2_{adj}	*p* Value	AIC	AICc	BIC	PRESS
1 July	Untransformed Model	PU = −36.50 + 41.79 NDVI+ 47.68 IRVI	0.44	<0.0001	173.86	174.00	184.85	542.23
	Transformed Model	log PU = −2.4161 − 2.0707 log (NDVI) − 1.2295 log (IRVI)	0.38	<0.0001	−285.14	−285.00	−274.15	106.82
12 July	Untransformed Model	PU = −9.68 NDVI − 4.39 IRVI	0.27	<0.0001	252.38	252.52	263.37	688.01
	Transformed Model	log PU = −1.0494 − 1.7365 log (NDVI) − 0.4754 log (IRVI)	0.24	<0.0001	−227.39	−227.56	−216.40	129.91
18 July	Untransformed Model	PU = −50.48 + 55.22 NDVI + 73.44 IRVI	0.13	<0.0001	303.82	303.96	314.81	827.77
	Transformed Model	log PU = 0.3755 − 0.9971 log (NDVI)	0.01	0.0450	−156.04	−155.96	−148.72	167.53
1 August	Untransformed Model	PU = 0.3387 + 18.9722 IRVI	0.28	<0.0001	247.15	247.23	254.47	678.70
	Transformed Model	log PU = 2.8567 + 0.9853 log (IRVI)	0.24	<0.0001	−229.51	−229.42	−222.18	129.49

NDVI: Normalized difference vegetation index; IRVI: Inverse infrared vegetative index; Akaike's Information Criterion (AIC); AICc: Akaike's Information Corrected Criterion; BIC: Bayesian Information Criterion. Significantly different at *p* < 0.05. PRESS: Prediction sum of squares.

Table 8. Total potato yield models with adjusted coefficient of determination (R^2_{adj}), *p* Value, AIC, AICc, BIC, and PRESS for flight operations.

Flights	Model Transformation	Model	R^2_{adj}	*p* Value	AIC	AICc	BIC	PRESS
25 June	Untransformed Model	Yield = 45.89 − 45.18 NDVI + 15.36 CHLGR − 23.76 ANTHO	0.50	<0.0001	431.90	432.41	443.05	4407.10
	Transformed Model	Log Yield = 1.6472 − 0.6025 NDVI − 0.7942 GNDVI + 1.2772 CHLGR − 0.5067	0.63	<0.0001	−635.72	−635.21	−624.57	6.05
1 July	Untransformed Model	Yield = 23.7808+ 0.4786 GNDVI + 5.5628 CHLGR − 1.3306 ANTHO + 41.30	0.44	<0.0001	453.57	454.09	464.72	5230.18
	Transformed Model	log Yield = 1.3201 + 0.7931 GNDVI − 0.7896 BNDVI + 0.1904 CHLGR − 0.1534 ANTHO	0.44	<0.0001	−630.53	−629.80	−616.60	6.58
9 July	Untransformed Model	Yield = 25.13 + 78.91 NDVI − 166.03 GNDVI + 34.67 BNDVI + 13.10 CHLGR + 10.53 ANTHO	0.56	<0.0001	419.10	420.09	435.83	3977.76
	Transformed Model	Log Yield = 1.179 + 0.973 NDVI − 2.074 GNDVI + 0.405 BNDVI + 0.155 CHLGR + 0.137 ANTHO	0.55	<0.0001	−655.38	−654.39	−638.65	5.18
16 July	Untransformed Model	Yield = 45.037 + 91.383 GNDVI − 76.667 BNDVI	0.47	<0.0001	437.26	437.60	445.62	4543.39
	Transformed Model	Log Yield = 1.381 + 1.075 GNDVI − 0.896 BNDVI	0.50	<0.0001	−645.75	−645.41	−637.39	5.66
22 July	Untransformed Model	Yield = 45.792 − 38.086 NDVI − 89.254 GNDVI + 3.923 BNDVI + 46.422 CHLGR	0.40	<0.0001	454.06	454.79	468.00	5189.32
	Transformed Model	Log Yield = 1.379 − 0.416 NDVI − 0.787 GNDVI + 0.012 BNDVI + 0.446 CHLGR	0.42	<0.0001	−625.11	−624.38	−611.18	6.61
29 July	Untransformed Model	Yield = 46.12 − 14.56 BNDVI + 5.06 CHLGR − 24.14 ANTHO − 15.60 GNDVI	0.52	<0.0001	427.69	428.21	438.84	4204.66
	Transformed Model	Log Yield = 1.284 + 0.100 NDVI + 0.988 GNDVI − 0.767 BNDVI − 0.147 ANTHO	0.54	<0.0001	−654.51	−653.78	−640.57	5.27
14 August	Untransformed Model	Yield = 9.814 + 42.583 NDVI + 109.470 GNDVI − 78.826 BNDVI − 4.019 CHLGR	0.37	<0.0001	459.88	460.61	473.81	5444.55
	Transformed Model	Log Yield = 0.896 + 0.582NDVI + 0.488 GNDVI − 0.531 BNDVI	0.34	<0.0001	−610.86	−610.34	−599.71	7.47
23 August	Untransformed Model	Yield = 53.300 − 12.472 NDVI + 0.013 GNDVI − 17.562 BNDVI + 0.439 CHLGR − 20.053 ANTHO	0.47	0.0012	441.78	442.78	442.77	4970.32
	Transformed Model	Log Yield = 1.487 − 1.069 NDVI + 1.610 GNDVI − 2.421 BNDVI − 1.898 ANTHO	0.45	<0.0001	−631.00	−630.81	615.07	6.50

NDVI: Normalized difference vegetation index; BNDVI: Blue NDVI: GNDVI: Green NDVI; CHLGR: Chlorophyll green; ANTHO: Anthocyanin; Akaike's Information Criterion (AIC); AICc: Akaike's Information Corrected Criterion; BIC: Bayesian Information Criterion. Significantly different at *p* < 0.05; PRESS: Prediction sum of squares.

Table 9. Phosphorus uptake (kg ha $^{-1}$) models with the adjusted coefficient of determination (R^2_{adj}), *p* Value, AIC, AICc, BIC, and PRESS for flight operations.

Flights	Model Transformation	Model	R^2_{adj}	*p* Value	AIC	AICc	BIC	PRESS
9 July	Untransformed Model	PU = 5.695 − 1.0549 NDVI + 4.686 GNDVI − 4.0981 BNDVI	0.12	0.0003	3.55	4.07	14.70	125.13
	Transformed Model	Log PU = 0.594 − 0.143 NDVI + 0.894 GNDVI − 0.820 BNDVI	0.17	<0.0001	−428.41	−4.27	−417.26	6.54
16 July	Untransformed Model	PU = 3.123 + 1.738 NDVI	0.10	0.0002	4.25	4.45	9.83	124.03
	Transformed Model	Log PU = 1.122 + 0.444 NDVI	0.13	<0.0001	−348.79	−348.58	−343.21	6.54
22 July	Untransformed Model	PU = 3.094 + 2.033 NDVI − 0.619 BNDVI + 2.980 ANTHO	0.06	0.003	7.53	8.51	24.26	126.57
	Transformed Model	Log PU = 1.0377 + 0.4322 NDVI + 0.797 ANTHO	0.07	0.004	−346.07	−345.34	−332.13	6.65
29 July	Untransformed Model	PU = 2.808 + 1.228 NDVI + 0.615 BNDVI + 1.975 ANTHO	0.12	0.02	3.88	4.40	15.03	123.97
	Transformed Model	Log PU = 0.988 − 0.335 NDVI − 2.071 GNDVI + 1.511 BNDVI + 0.586 ANTHO	0.15	<0.0001	−348.91	−348.18	−334.97	6.48
14 August	Untransformed Model	PU = 4.525 − 15.386 GNDVI + 8.289 BNDVI + 0.4802 CHLGR	0.15	<0.0001	2.36	3.34	11.37	123.12
	Transformed Model	Log PU = 1.497 − 3.579 GNDVI + 1.934 BNDVI + 0.0972 CHLGR	0.17	<0.0001	−352.56	−352.04	−341.41	6.48

NDVI: Normalized difference vegetation index; BNDVI: Blue NDVI: GNDVI: Green NDVI; CHLGR: Chlorophyll green; ANTHO: Anthocyanin; Akaike's Information Criterion (AIC); AICc: Akaike's Information Corrected Criterion; BIC: Bayesian Information Criterion. Significantly different at *p* < 0.05; PRESS: Prediction sum of squares; PU: Phosphorus uptake.

3.2.2. Relationships between Actual and Predicted Variables

Models built using the data obtained by the passive sensors showed stronger and more consistent correlations between the actual and predicted total potato yields than the models based on the data from active sensors. The strongest relationship between the actual and predicted total potato yield was obtained by the transformed model for the first drone flight on 25 June, with an adjusted R^2 of 0.63 (Figure 8b). For other models, the coefficients of determination fluctuated between 0.50 and 0.56. On the other hand, the phosphorous uptake data showed little correlation between the actual and predicted values (Figure 9).
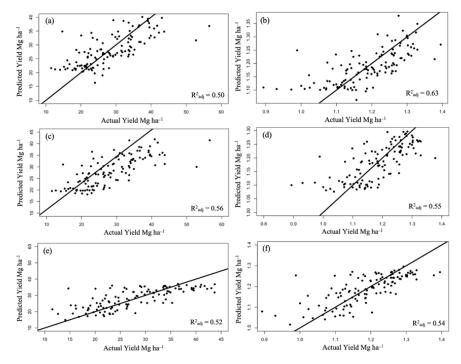

Figure 8. Relationship between the actual and predicted total potato yield for (**a**) the first flight on 25 June, the untransformed model; (**b**) the first flight on 25 June, the transformed model; (**c**) the third flight on 9 July, the untransformed model; (**d**) third flight on 9 July, the transformed model; (**e**) the sixth flight on 29 July, the untransformed model; (**f**) the sixth flight on 29 July, the transformed model.
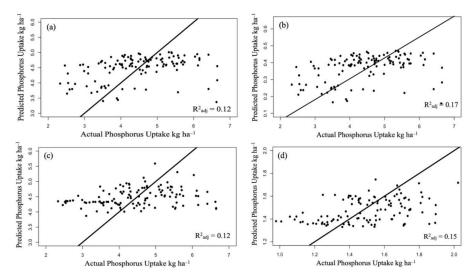

Figure 9. Relationship between the actual and predicted phosphorus uptake for (**a**) the third flight on 9 July, the untransformed model; (**b**) the third flight on 9 July, the transformed model; (**c**) the sixth flight on 29 July, the untransformed model; (**d**) the sixth flight on 29 July, the transformed model.

4. Discussion

Understanding the relationships and correlations between yield and phosphorous application requires assessing different sites with different vegetation indices and plant pigments [11]. The NIR region plays a vital role in predicting phosphorus stress due to the internal leaf structure; under P stress, the number of small leaf cells is increased compared to non-stress conditions [11,58].

Indices obtained by the Crop Circle™ active sensor were weakly correlated with total potato yield, most likely because the Crop Circle™ active sensor can be more sensitive to nitrogen stress than to P stress [12,59]. The highest amount of variation explained by the model was only 36% (R^2_{adj} = 0.36), achieved at the first sensing date (25 June). After that, the fitted models' explanatory capabilities dropped (Table 6). In contrast, 60% of the variation in P uptake (R^2_{adj} = 0.60) could be explained by the model on the third sensing date (9 July). However, subsequently, sensor performance deteriorated (Table 7). This could be attributed to potato tissue phosphorus that could be decreased at the end of the season growth stages due to the P translocation from the shoot system to tubers regardless of the soil P concentration, which could exhibit a vast P stress [15,60].

Correlations between the actual and predicted variables revealed the poor predictive abilities of Crop Circle™ regarding the total potato yield, as well as being only a moderate predictive model for P uptake. This could be attributed to the values of NDVI, which were lower than those at NDRE due to the red band, which was not useful to predict phosphorus stress and the overlapping between plant pigment reflectance [15].

For the GreenSeeker™ active sensor output, the adjusted R^2 values were weak to moderate for NDVI and IRVI at all dates. This might be because the GreenSeeker active sensor operates in two wavelengths centered at the red and NIR with no red-edge. The red-edge band can predict P in crops [61]. The GreenSeeker™ active sensor readings showed a weak relationship with potato yield and P uptake when used individually. Similar to Crop Circle™, it was a useful sensor for nitrogen rather than phosphorus [12,62].

In this study, the vegetation indices derived from passive sensors showed a better correlation with total potato yield than the active sensors, which might be due to the extraction and analysis of the images based on removing the soil and other non-plant pixels before calculating the vegetation indices using the passive sensors [63,64]. At the first flight, the ANTHO and NDVI were negatively correlated with total potato yield, with a moderate adjusted R^2 (0.50), and positively correlated during the third drone flight, with an adjusted R^2 of 0.56. ANTHO was estimated from the red band and green band's reflectance ratio to reduce the overlap between the ANTHO and chlorophyll [17]. However, there are two possible explanations for this result. Firstly, the leaf surface reflectance in the visible region is larger than that in the infrared region. Secondly, the ANTHO content is high at the early vegetative stage, characterized by low photosynthetic activity [13]. At the early and late leaf stages, the green band might have a lower reflectance (higher absorption) than the middle stage of the growing season [14,21].

P uptake was not successfully determined by the models created based on the passive sensor data. During the flights, the adjusted R^2 values ranged from 0.06 to 0.17. Even though the transformed methods reinforced the equations, the models were still considered poor predictive models. However, early potato stages, such as vegetative growth (30 days after planting) and tuber initiation (50–60 days after planting), are important stages for the plants to accumulate sufficient soil P, which can be reflected in potato growth [6,60]. At the end of the potato growing season, the cell number, shape, size, and water content decrease, leading to increased absorption at the green band and increased blue and red reflectance. Furthermore, plant stress at the end of the potato growing season could be confounded with plant senescence [18]. Additionally, there is no huge P stress at the late potato growth stage due to the high soil P, thus, P stress would be rarely detected by the sensors [15].

5. Conclusions

This study assessed the employment of active sensing (Crop Circle™ and GreenSeeker™) and passive sensing (multispectral imaging with UAVs) to predict total potato yield and P uptake. The vegetation

indices were calculated from the data collected by the active and passive sensors to generate the models. The vegetation indices developed using Crop Circle™ showed weak correlations with total potato yield but were good in providing an early season estimate of P uptake. Similar results were observed using GreenSeeker™. GreenSeeker™ is also moderately effective in predicting P uptake early in the season. The passive sensor data extracted from visible and multispectral imagery provide good estimates of total potato yield at the early potato season and can be used to predict P stress though it predicted P uptake only late in the season. The remotely sensed imagery showed a significant correlation between total potato yield and the NDVI, CHLGR, and ANTHO indices. However, it was largely useless in predicting P uptake. Future investigations should assess these results on soils with different P concentrations, under different environmental conditions, and using different active and passive sensors.

Author Contributions: A.J., L.K.S., A.A., C.W. and S.K.B. designed, collected and analyzed data, and wrote the manuscript. A.Z. and A.B. collected soil, and plant data; L.K.S. and A.A. acquired the funding. All authors have read and agreed to the published version of the manuscript.

Conflicts of Interest: The authors declare no conflict of interest.

References

1. Greenway, G.A.; Guenthner, J.F.; Makus, L.D.; Pavek, M.J. An Analysis of Organic Potato Demand in the U.S. *Am. J. Potato Res.* **2010**, *88*, 184–189. [CrossRef]
2. USDA. *United States Department of Agriculture National Resources Conservation Service*; The PLANTS Database, National Plant Data Center: Baton Rouge, LA, USA, 2018.
3. Abbasian, A.; Ahmadi, A.; Abbasi, A.; Darvishi, B. Effect of various phosphorus and calcium concentrations on potato seed tuber production. *J. Plant Nutr.* **2018**, *41*, 1765–1777. [CrossRef]
4. Fernandes, A.M.; Soratto, R.P.; Pilon, C. Soil Phosphorus Increases Dry Matter and Nutrient Accumulation and Allocation in Potato Cultivars. *Am. J. Potato Res.* **2014**, *92*, 117–127. [CrossRef]
5. Osborne, S.L. Separating Spectral Signatures for Detecting Nitrogen, Phosphorus and Water Stress in Corn. Ph.D. Thesis, University of Nebraska, Lincoln, NE, USA, 1999.
6. Havlin, J.L.; Tisdale, S.L.; Nelson, W.L.; Beaton, J.D. *Soil Fertility and Fertilizers*; Pearson Education India, Inc.: Upper Saddle River, NJ, USA, 2016.
7. Barker, A.V.; Pilbeam, D.J. *Handbook of Plant Nutrition*; CRC Press: Boca Raton, FL, USA, 2015.
8. Duff, S.M.; Sarath, G.; Plaxton, W.C. The role of acid phosphatases in plant phosphorus metabolism. *Physiol. Plant.* **1994**, *90*, 791–800. [CrossRef]
9. Wang, Z.Q.; Zhou, X.; Dong, L.; Guo, J.; Chen, Y.; Zhang, Y.; Wu, L.; Xu, M. iTRAQ-based analysis of the Arabidopsis proteome reveals insights into the potential mechanisms of anthocyanin accumulation regulation in response to phosphate deficiency. *J. Proteom.* **2018**, *184*, 39–53. [CrossRef] [PubMed]
10. Mahajan, G.; Sahoo, R.; Pandey, R.; Gupta, V.; Kumar, D. Using hyperspectral remote sensing techniques to monitor nitrogen, phosphorus, sulphur and potassium in wheat (*Triticum aestivum* L.). *Precis. Agric.* **2014**, *15*, 499–522. [CrossRef]
11. Osborne, S.L.; Schepers, J.S.; Francis, D.D.; Schlemmer, M.R. Detection of Phosphorus and Nitrogen Deficiencies in Corn Using Spectral Radiance Measurements. *Agron. J.* **2002**, *94*, 1215–1221. [CrossRef]
12. Sharma, L.; Bu, H.; Franzen, D.; Denton, A. Use of corn height measured with an acoustic sensor improves yield estimation with ground based active optical sensors. *Comput. Electron. Agric.* **2016**, *124*, 254–262. [CrossRef]
13. A Sims, D.; A Gamon, J. Relationships between leaf pigment content and spectral reflectance across a wide range of species, leaf structures and developmental stages. *Remote. Sens. Environ.* **2002**, *81*, 337–354. [CrossRef]

14. Gitelson, A.A.; Merzlyak, M.N. Non-destructive assessment of chlorophyll carotenoid and anthocyanin content in higher plant leaves: Principles and algorithms. *Remote. Sens. Agric. Environ.* **2004**, 78–94. Available online: https://digitalcommons.unl.edu/cgi/viewcontent.cgi?article=1265&context=natrespapers (accessed on 10 February 2020).

15. Osborne, S.L.; Schepers, J.S.; Schlemmer, M.R. Detecting Nitrogen and Phosphorus Stress in Corn Using Multi-spectral Imagery. *Commun. Soil Sci. Plant Anal.* **2004**, *35*, 505–516. [CrossRef]

16. Hunt, E.R.; Daughtry, C.S.T.; Mirsky, S.B.; Hively, W.D. Remote Sensing With Simulated Unmanned Aircraft Imagery for Precision Agriculture Applications. *IEEE J. Sel. Top. Appl. Earth Obs. Remote. Sens.* **2014**, *7*, 4566–4571. [CrossRef]

17. Gamon, J.A.; Surfus, J.S. Assessing leaf pigment content and activity with a reflectometer. *New Phytol.* **1999**, *143*, 105–117. [CrossRef]

18. Carroll, M.W.; Glaser, J.A.; Hellmich, R.L.; Hunt, T.E.; Sappington, T.W.; Calvin, D.; Copenhaver, K.; Fridgen, J. Use of spectral vegetation indices derived from airborne hyperspectral imagery for detection of European corn borer infestation in Iowa corn plots. *J. Econ. Entomol.* **2008**, *101*, 1614–1623. [CrossRef] [PubMed]

19. Soundararajan, M. Relationship between leaf chlorophyll content and carbon isotope discrimination in soybean. *IPCBEE* **2012**, *31*, 22–27.

20. Gitelson, A.A.; Gamon, J.A.; Solovchenko, A. Multiple drivers of seasonal change in PRI: Implications for photosynthesis 1. Leaf level. *Remote. Sens. Environ.* **2017**, *191*, 110–116. [CrossRef]

21. Gitelson, A.A.; Keydan, G.; Merzlyak, M.N. Three-band model for noninvasive estimation of chlorophyll, carotenoids, and anthocyanin contents in higher plant leaves. *Geophys. Res. Lett.* **2006**, *33*, 11. [CrossRef]

22. Holland, K.H.; Lamb, D.; Schepers, J.S. Radiometry of Proximal Active Optical Sensors (AOS) for Agricultural Sensing. *IEEE J. Sel. Top. Appl. Earth Obs. Remote Sens.* **2012**, *5*, 1793–1802. [CrossRef]

23. Barker, D.W.; Sawyer, J.E. Factors Affecting Active Canopy Sensor Performance and Reflectance Measurements. *Soil Sci. Soc. Am. J.* **2013**, *77*, 1673–1683. [CrossRef]

24. Kipp, S.; Mistele, B.; Schmidhalter, U. The performance of active spectral reflectance sensors as influenced by measuring distance, device temperature and light intensity. *Comput. Electron. Agric.* **2014**, *100*, 24–33. [CrossRef]

25. Hatfield, J.L.; Prueger, J.H. Value of Using Different Vegetative Indices to Quantify Agricultural Crop Characteristics at Different Growth Stages under Varying Management Practices. *Remote Sens.* **2010**, *2*, 562–578. [CrossRef]

26. Yu, K.; Li, F.; Gnyp, M.L.; Miao, Y.; Bareth, G.; Chen, X. Remotely detecting canopy nitrogen concentration and uptake of paddy rice in the Northeast China Plain. *ISPRS J. Photogramm. Remote Sens.* **2013**, *78*, 102–115. [CrossRef]

27. Cao, Q.; Miao, Y.; Feng, G.; Gao, X.; Li, F.; Liu, B.; Yue, S.; Cheng, S.; Ustin, S.L.; Khosla, R. Active canopy sensing of winter wheat nitrogen status: An evaluation of two sensor systems. *Comput. Electron. Agric.* **2015**, *112*, 54–67. [CrossRef]

28. Eitel, J.U.H.; Keefe, R.F.; Long, D.S.; Davis, A.S.; Vierling, L.A. Active Ground Optical Remote Sensing for Improved Monitoring of Seedling Stress in Nurseries. *Sensors* **2010**, *10*, 2843–2850. [CrossRef] [PubMed]

29. Li, F.; Mistele, B.; Hu, Y.; Yue, X.; Yue, S.; Miao, Y.; Chen, X.; Cui, Z.; Meng, Q.; Schmidhalter, U. Remotely estimating aerial N status of phenologically differing winter wheat cultivars grown in contrasting climatic and geographic zones in China and Germany. *Field Crop. Res.* **2012**, *138*, 21–32. [CrossRef]

30. Shaver, T.M.; Khosla, R.; Westfall, D.G. Evaluation of Two Ground-Based Active Crop Canopy Sensors in Maize: Growth Stage, Row Spacing, and Sensor Movement Speed. *Soil Sci. Soc. Am. J.* **2010**, *74*, 2101–2108. [CrossRef]

31. Cao, Q.; Miao, Y.; Shen, J.; Yu, W.; Yuan, F.; Cheng, S.; Huang, S.; Wang, H.; Yang, W.; Liu, F. Improving in-season estimation of rice yield potential and responsiveness to topdressing nitrogen application with Crop Circle active crop canopy sensor. *Precis. Agric.* **2015**, *17*, 136–154. [CrossRef]

32. Scientifc, H. 2020. Available online: https://hollandscientific.com/portfolio/crop-circle-acs-430/ (accessed on 11 September 2020).

33. Wang, T.; Thomasson, J.A.; Yang, C.; Isakeit, T.; Nichols, R.L. Automatic Classification of Cotton Root Rot Disease Based on UAV Remote Sensing. *Remote Sens.* **2020**, *12*, 1310.

34. Li, S.; Ding, X.; Kuang, Q.; Ata-Ui-Karim, S.T.; Cheng, T.; Liu, X.; Tian, Y.; Zhu, Y.; Cao, W.; Cao, Q. Potential of UAV-Based Active Sensing for Monitoring Rice Leaf Nitrogen Status. *Front. Plant Sci.* **2018**, *9*, 1834. [CrossRef]

35. Carlson, T.N.; Ripley, D.A. On the relation between NDVI, fractional vegetation cover, and leaf area index. *Remote Sens. Environ.* **1997**, *62*, 241–252. [CrossRef]

36. Rouse, J.W., Jr.; Haas, R.; Schell, J.; Deering, D. Monitoring vegetation systems in the Great Plains with ERTS. In Proceedings of the Third Earth Resources Technology Satellite-1 Symposium, Greenbelt, MD, USA, 1 January 1974; p. 371.

37. Milton, N.; Eiswerth, B.; Ager, C. Effect of phosphorus deficiency on spectral reflectance and morphology of soybean plants. *Remote Sens. Environ.* **1991**, *36*, 121–127. [CrossRef]

38. Shi, J.; Zou, X.; Zhao, J.; Mao, H.; Wang, K.; Chen, Z.; Huang, X.; Holmes, M. Pre-Visual Diagnostics of Phosphorus Deficiency in Mini-Cucumber Plants Using Near-Infrared Reflectance Spectroscopy. *Appl. Spectrosc.* **2012**, *66*, 1426–1432. [CrossRef] [PubMed]

39. Li, L.; Wang, S.; Ren, T.; Wei, Q.; Ming, J.; Li, J.; Li, X.; Cong, R.; Lu, J. Ability of models with effective wavelengths to monitor nitrogen and phosphorus status of winter oilseed rape leaves using in situ canopy spectroscopy. *Field Crop. Res.* **2018**, *215*, 173–186. [CrossRef]

40. Mahajan, G.R.; Pandey, R.N.; Sahoo, R.N.; Gupta, V.K.; Datta, S.C.; Kumar, D. Monitoring nitrogen, phosphorus and sulphur in hybrid rice (*Oryza sativa* L.) using hyperspectral remote sensing. *Precis. Agric.* **2017**, *18*, 736–761. [CrossRef]

41. Zhu, W.; Huang, Y.; Sun, Z. Mapping Crop Leaf Area Index from Multi-Spectral Imagery Onboard an Unmanned Aerial Vehicle. In Proceedings of the 2018 7th International Conference on Agro-Geoinformatics (Agro-Geoinformatics), Hangzhou, China, 6–9 August 2018; pp. 1–5.

42. Extension, C. Maine Board of Pesticides Control—Cooperative Extension: Potatoes—University of Maine Cooperative Extension. 2018. Available online: https://extension.umaine.edu/potatoes/recertification-credits/maine-board-of-pesticides-control/ (accessed on 16 October 2018).

43. McLean, E. Soil pH and lime requirement. In *Methods of Soil Analysis. Part 2. Chemical and Microbiological Properties*; American Society of Agronomy: Madison, WI, USA, 1982; pp. 199–224.

44. Storer, D.A. A simple high sample volume ashing procedure for determination of soil organic matter. *Commun. Soil Sci. Plant Anal.* **1984**, *15*, 759–772. [CrossRef]

45. Mehlich, A. Mehlich 3 soil test extractant: A modification of Mehlich 2 extractant. *Commun. Soil Sci. Plant Anal.* **1984**, *15*, 1409–1416. [CrossRef]

46. Keeney, D.R.; Nelson, D.W. *Methods of Soil Analysis. Part 2. Chemical and Microbiological Properties*, 2nd ed.; American Society of Agronomy: Madison, WI, USA, 1982; pp. 643–698.

47. Dahnke, W.C.; Whitney, D.A. Measurement of soil salinity. *Recomm. Chem. Soil Test Proced. N. Cent. Reg.* **1988**, *221*, 32–34.

48. Westermann, D.T.; Kleinkopf, G.E. Phosphorus Relationships in Potato Plants 1. *Agron. J.* **1985**, *77*, 490–494. [CrossRef]

49. Chapman, H.D.; Pratt, P.F. Methods of Analysis for Soils, Plants and Waters. *Soil Sci.* **1962**, *93*, 68. [CrossRef]

50. Kalra, Y.P.; Maynard, D.G. *Methods Manual for Forest Soil and Plant Analysis, Information Report NOR-X-319E*; Northern Forestry Center, Northwest Region: Edmonton, AB, Canada, 1991; Volume 319.

51. Xing, L.; Pittman, J.J.; Inostroza, L.; Butler, T.J.; Munoz, P. Improving Predictability of Multisensor Data with Nonlinear Statistical Methodologies. *Crop. Sci.* **2018**, *58*, 972–981. [CrossRef]

52. Bendig, J.; Bolten, A.; Bareth, G. UAV-based Imaging for Multi-Temporal, very high Resolution Crop Surface Models to monitor Crop Growth Variability Monitoring des Pflanzenwachstums mit Hilfe multitemporaler und hoch auflösender Oberflächenmodelle von Getreidebeständen auf Basis von Bildern aus UAV-Befliegungen. *Photogramm. Fernerkund. Geoinf.* **2013**, *2013*, 551–562.

53. Pix4D Mapper. 2019. Available online: https://www.pix4d.com/product/pix4dmapper-photogrammetry-software (accessed on 15 January 2019).

54. Agisoft Metashape Professional. 2020. Available online: https://www.agisoft.com/downloads/installer/ (accessed on 10 January 2020).

55. ArcGIS 10.3. 2019. Available online: www.arcgis.com (accessed on 20 February 2019).

56. A Gitelson, A.; Merzlyak, M.N. Spectral Reflectance Changes Associated with Autumn Senescence of *Aesculus hippocastanum* L. and *Acer platanoides* L. Leaves. Spectral Features and Relation to Chlorophyll Estimation. *J. Plant Physiol.* **1994**, *143*, 286–292. [CrossRef]

57. Wang, F.-M.; Huang, J.H.; Tang, Y.-L.; Wang, X.-Z. New Vegetation Index and Its Application in Estimating Leaf Area Index of Rice. *Rice Sci.* **2007**, *14*, 195–203. [CrossRef]

58. Junior, C.K.; Guimarães, A.M.; Caires, E.F. Use of active canopy sensors to discriminate wheat response to nitrogen fertilization under no-tillage. *Eng. Agríc.* **2016**, *36*, 886–894. [CrossRef]

59. Jacob, J.; Lawlor, D.W. Stomatal and Mesophyll Limitations of Photosynthesis in Phosphate Deficient Sunflower, Maize and Wheat Plants. *J. Exp. Bot.* **1991**, *42*, 1003–1011. [CrossRef]

60. Sharma, L.K.; Bali, S.K.; Dwyer, J.D.; Plant, A.B.; Bhowmik, A. A Case Study of Improving Yield Prediction and Sulfur Deficiency Detection Using Optical Sensors and Relationship of Historical Potato Yield with Weather Data in Maine. *Sensors* **2017**, *17*, 1095. [CrossRef]

61. Hopkins, B.G.; Hansen, N.C. Phosphorus Management in High-Yield Systems. *J. Environ. Qual.* **2019**, *48*, 1265–1280. [CrossRef]

62. Sembiring, H.; Raun, W.; Johnson, G.V.; Stone, M.L.; Solie, J.B.; Phillips, S.B. Detection of nitrogen and phosphorus nutrient status in bermudagrass using spectral radiance. *J. Plant Nutr.* **1998**, *21*, 1189–1206. [CrossRef]

63. Sharma, L.K.; Bali, S.; Zaeen, A.; Baldwin, P.; Franzen, D. Use of Rainfall Data to Improve Ground-Based Active Optical Sensors Yield Estimates. *Agron. J.* **2018**, *110*, 1561–1571. [CrossRef]

64. Hunt, E.R.; Daughtry, C.S.T.; Eitel, J.U.H.; Long, D.S. Remote Sensing Leaf Chlorophyll Content Using a Visible Band Index. *Agron. J.* **2011**, *103*, 1090–1099. [CrossRef]